**Classification:** Biological Sciences, Neuroscience

# Morphological Adaptations of Mitochondria in Spatially Restricted Axons Revealed by Cryo-Electron Tomography

Tara D. Fischer[1,†], Pramod K. Dash[1,2], Jun Liu[1,‡], and M. Neal Waxham[1*]

**Author Affiliations:**

[1]Department of Neurobiology and Anatomy, McGovern Medical School, University of Texas Health Science Center at Houston, Houston, TX 77030

[2]Vivian L. Smith Department of Neurosurgery, McGovern Medical School, University of Texas Health Science Center at Houston, Houston, TX 77030

Present Address:

[†]Biochemistry Section, Surgical Neurology Branch, National Institute of Neurological Disorders and Stroke, National Institutes of Health, Bethesda, MD 20892

[‡]Department of Microbial Pathogenesis & Microbial Sciences Institute, Yale School of Medicine, New Haven, CT 06519

***Corresponding Author:** M. Neal Waxham. 6431 Fannin st., MSB 7.254, Houston, TX 77030. (713) 500-5621. m.n.waxham@uth.tmc.edu

**Keywords:** Cryo-electron tomography, mitochondria, mitochondrial transport, mitochondrial membranes

**Abstract**

Neurons project axons to local and distal sites that can display heterogeneous morphologies with restricted physical dimensions that may influence the transport of large organelles, such as mitochondria. Although transport of mitochondria has been widely studied, whether spatial constraints within axons determines the distribution or morphological characteristics of mitochondria has not been systematically examined. The current study provides insight into the spatial environments of mitochondria within axons and presynaptic varicosities of cryopreserved hippocampal neurons imaged in their native state using 3D cryo-electron tomography (cryo-ET). Segmented tomographic reconstructions revealed major morphological adaptations of mitochondria due to restricted physical dimensions at the boundary between presynaptic varicosities and axons. Furthermore, segmentation of individual mitochondrial membranes revealed distinct structural changes between the inner and outer membranes during this modification, suggesting independent regulation of each membrane to adapt to the spatial constraints within axons. These findings offer a new perspective on the remarkable structural plasticity of mitochondrial membranes and the adaptability of mitochondrial morphology to navigate limited available space necessary for axonal transport.

**Significance Statement**

Restrictive physical dimensions within axons pose a significant problem as to how rather large organelles, such as mitochondria, navigate the constrained space for efficient axonal transport. Using cryo-electron tomography, we characterized native spatial environments within axons and presynaptic varicosities of hippocampal neurons to determine whether the magnitude of spatial restrictions within these compartments may influence the subcellular distribution and morphology of mitochondria. Major morphological adaptations of mitochondria and their membranes were revealed due to restricted available space within axons. These findings offer new perspectives on the influence of physical and spatial characteristics of cellular environments on mitochondrial morphology and highlights the remarkable structural plasticity of mitochondria to navigate the limited available space during axonal transport.

## Introduction

Neurons are architecturally complex cells that can extend axonal projections with elaborate arborization for several hundreds of millimeters (and in some cases, meters) to form synaptic connections with local and distal targets (1-3). Depending on the target, presynaptic compartments can either be found at the end of axons (terminal boutons) or tracking along axons as intermediate swellings (*en passant* boutons or varicosities), such as in the unmyelinated CA3->CA1 axons of the hippocampus (3-7). The bead-like presynaptic varicosities are morphologically heterogeneous, displaying diameters that can range from 1-2 μm connected by thin axon segments that can have diameters less than 100 nm (4, 5, 8, 9).

Tracking through the axons is a well-developed system of microtubules that mediate motor-driven anterograde and retrograde transport of signaling cargoes, protein complexes and organelles critical for function and homeostasis at distant synapses (10, 11). Transport of these intracellular components creates a spatially and temporally dynamic axonal environment that can contain a variety of organelles and cargoes of different shapes, sizes, and number (12, 13). As the axon segments interconnecting varicosities can be remarkably thin and the available space within axons can be occupied by various organelles and cargo, their overall diameter and changes in internal volume present an interesting problem for the efficient transport of large organelles, such as mitochondria, that can display an average diameter between 100-500 nm (14, 15). Axonal transport of mitochondria is particularly critical for synaptic development, function, and plasticity and movement is known to make frequent stops, or saltatory movements, at presynaptic compartments to provide local ATP synthesis and calcium regulation required for proper neurotransmission (16-20). Given the morphological complexity of axons, restricted physical dimensions and available space could potentially influence the subcellular localization, distribution, and transport of mitochondria required to meet local energy needs and for supporting synaptic transmission. Although mitochondria are morphologically dynamic organelles that can exist in a variety of shapes and sizes, how mitochondria adapt to the physical constraints presented in axons to navigate the spatially restricted environment has not been previously examined.

Advances in microscopy and imaging techniques have played a pivotal role in revealing the three-dimensional architecture of neurons and their intracellular environments at resolutions reaching the nanometer scale (21, 22). In the current study, we employed the unique native state preservation afforded by cryopreservation and the

resolution provided by cryo-electron tomography (cryo-ET) to visualize three-dimensional spatial relationships and organellar structure within cultured hippocampal axons. Our results show that axon morphology and physically restrictive intracellular dimensions present a previously unrecognized influence on mitochondria residing within axonal subcompartments, revealing dramatic adaptations mitochondria must undertake to navigate the available space during transport.

## Results

### Preparation of primary hippocampal neurons for cryo-ET

Primary neuronal cultures from E18 rat hippocampi were grown on holey carbon grids prior to cryo-preservation. At 10 days post plating, primary hippocampal neurons have extended dendritic and axonal processes and have established pre-synaptic varicosities and initial excitatory synaptic connections (23). **Figure 1A** and **B** show representative bright field images of neurons cultured on a Quantifoil grid where widespread elaboration of processes is evident. **Figure 1C** and **D** demonstrate images of companion grids that were fixed and immunolabeled with antibodies to calcium/calmodulin dependent protein kinase II alpha (CaMKII$\alpha$) and synapsin 1 to visualize the excitatory neuron population and presynaptic varicosities, respectively. CaMKII□ largely labels soma and processes, while the synapsin 1 antibody shows distinct puncta representing enrichment of synaptic vesicles at presynaptic varicosities.

For cryo-ET, fiducial gold markers were applied to prepared grids and cryopreserved by plunge freezing in liquid ethane. Cryopreservation conserves the near native state of the preparation permitting a fixation free assessment of spatial relationships of organelles present in different intracellular environments within hippocampal neurons. Low magnification images were first collected (**Fig. 1E**) and montaged to provide maps for targeting areas of interest for data collection. A higher magnification image reveals the distribution of presynaptic varicosities and axonal processes (**Fig. 1F**). Varicosities and axons can be seen residing on both the carbon and overlying the grid holes. To provide maximum contrast, tomographic data collection was targeted to cryopreserved structures within the grid holes. In these preparations, the increased thickness of the ice surrounding the soma and proximal dendrites prevented imaging of these structures. In contrast, the ice thickness surrounding the axonal processes and varicosities was ideal, permitting a detailed assessment of the spatial relationships of cytoskeletal structures and organelles within these subcompartments.

**Organelle populations of pre-synaptic varicosities in primary hippocampal neurons are heterogeneous**

Areas were randomly chosen, and tilt series were collected from varicosities and axon segments overlying grid holes to visualize cytoskeletal and organellar structures. **Figure 2A** shows a slice through a representative tomographic reconstruction with various resident organelles and structures visible, including two mitochondria, a multi-vesicular body (MVB), microtubules, endoplasmic reticulum (ER) and a collection of vesicles. To determine the three-dimensional (3D) relationship between the different structures, segmentation was accomplished of the tomographic reconstruction of both the presynaptic varicosity and the adjoining axon (**Fig. 2B; Movie S1**). The reconstruction demonstrates microtubules (light blue) forming a continuous set of tracks traveling from one end of the varicosity to the other. Microtubules appear less constrained within the varicosity where they exhibit greater curvature, while gathering together and straightening when entering the adjoining axon segment. The ER (yellow) also forms a reticulated and continuous structure spanning the entire length of the varicosity, consistent with other reports on the ubiquitous presence of ER in axons and synaptic terminals (21). Mitochondria, MVB, and Golgi, exhibit more random distributions within the varicosity, while vesicles appeared to be somewhat clustered. To determine if the presence of each of these identifiable organelles was consistent across varicosities, we analyzed their distribution in an additional 77 additional tomographic reconstructions. ER and microtubules were present in 100% of presynaptic varicosities, vesicles were present in 97%, mitochondria in 82%, Golgi bodies in 38%, multi-vesicular bodies in 21%, lamellar bodies in 9%, and autophagosomes in 4% (exemplars shown in **Fig. S1**). Variations in distinct sub-features of the observed organelle populations also emerged in 3D at high resolution. Specifically, the ubiquitous ER was observed in close apposition with almost every other organelle within the varicosities, consistent with ER-membrane contact sites described by others (21). The vesicular population was heterogeneous in number, ranging from 1 to >100 vesicles per varicosity. 75% of varicosities contained <50 vesicles, 10% had 50-100, and 6% contained greater than 100. Vesicles were observed in clusters with electron-dense filamentous connections (data not shown), consistent with previous reports of proteinaceous (synapsin, Bassoon, and or ERC2) tethering of synaptic vesicles (12, 13). Mitochondria were also often observed with variations in cristae morphology that could be broadly separated into two distinct populations based on ultrastructural features (**Fig. S2**).

A population of mitochondria displayed the canonical thin, tubular cristae morphology (**Fig. S2A**), while a second population displayed thick, unstructured cristae (**Fig. S2B**).

In contrast to the heterogeneous appearance and distribution of organelles in presynaptic varicosities, the adjoining axonal segments were more consistent in composition. The most obvious components were microtubules that were seen as continuous elements, gathered at the sites of axonal narrowing at both ends of the varicosity. Microtubules did not display variability in diameter (~20 nm), however they did vary in number among different tomograms and occupied a significant portion of the available volume within the axon (**Movie S2**). As noted, microtubules are the essential tracks required for motor driven organelle transport and are critical for maintaining synaptic homeostasis and neuronal signaling. The corresponding microtubule occupation of axonal space leaves the qualitative impression that the available volume in axons to accommodate organelles might be an under-appreciated constraint affecting transport.

**Mitochondria undergo major morphological changes in adaptation to spatial constraints within axons**

Previous EM studies have reported an average axonal diameter between 0.08 and 0.4 μm for unmyelinated cortical axons and an average varicosity diameter of ~1-2 μm (1, 5, 7, 8). The Feret diameters of axonal varicosities in our cryopreserved preparations exhibited an average of 650 nm (SD = 240 nm), and ranged from 250 nm to 1.65 μm (measured from 2D projections of cryopreserved varicosities; n = 200). Adjoining axon segments averaged 81 nm (SD = 27) in diameter and ranged between ~30-300 nm in Feret diameter (n = 195). Additionally, the average Feret diameters of mitochondria observed in varicosities was ~250 nm (n = 75), ranging between ~200 nm and ~430 nm. These dimensions further reinforce the idea that significant spatial constraints exist that must be overcome to permit mitochondrial transport through axonal processes. For more in-depth investigation of this issue, high magnification tomographic data were collected targeting mitochondria residing at the boundary where the varicosity narrows into the axonal segment. While such precise mitochondrial positioning was rare in the cryo-preserved neuronal population, the events that were captured revealed major mitochondrial morphological remodeling in adaptation to the constricted space in the adjoining axon segment. **Movie S3** demonstrates a mitochondrion partially residing in both a neuronal varicosity and the adjoining axon segment among the other organelles occupying space in these compartments. The portion of the mitochondrion residing in the

varicosity is 305 nm in Feret diameter, while the portion of the mitochondrion residing in the axonal segment has been reduced to only 70 nm in diameter. Thus, the mitochondrion displays a major morphological change with an approximately 77% reduction in diameter to adapt to the size of the axon. **Figure 3A** shows a snapshot of the segmented mitochondrion (see also **Movie S3)** as well as additional examples of mitochondria captured at the varicosity/axonal boundary (**Fig. 3B-D**). Analysis of eight mitochondria undergoing these drastic morphological changes revealed an average of 84% (n = 8, SD = 6%) reduction in the Feret diameter of the mitochondrial area in the varicosity relative to the adjoining axon segment. **Figure 3B** is particularly revealing, in which a mitochondrion was captured bridging a short (100 nm in length) axon segment between two varicosities. The morphological adaptation to this short narrowing space produced a barbell shaped mitochondrion with a diameter between 200-300 nm in both varicosities while the portion spanning the axon segment was only 19 nm in diameter. **Figure 3D** shows a reconstruction that revealed two mitochondria spanning the varicosity and adjoining axon segment, with a portion of a third mitochondrion residing entirely in the axon. This captured event highlights the adaptable nature of mitochondrial morphology, as demanded by the available space within an axon, to allow multiple mitochondria to undergo coordinated axonal transport. Note that in all of the segmented tomographic reconstructions in **Figure 3**, the presence of microtubules and additional organelles, such as the ER, further restricts the available volume that the mitochondria must navigate in axons.

**Mitochondrial membranes display distinct structural features during morphological adaptations to restricted space within axons**

Mitochondrial ultrastructure has been shown to have a dynamic architecture with remodeling of the inner membrane and formation of specified subcompartments, termed cristae (Cogliati et al., 2013; Cogliati, Enriquez, & Scorrano, 2016; Hackenbrock & Caplan, 1969). Given the major change in gross mitochondrial morphology we observed between varicosities and the adjoining axonal segments, we questioned if the inner mitochondrial membrane also undergoes significant remodeling to adapt to the reduction in axonal diameter. To address this issue, the outer and inner membranes of mitochondria caught in transition between varicosities and adjoining axons were segmented, separating the outer membrane, and two regional components of the IMM, the inner boundary membrane (IBM) and the cristae. A conservative approach was taken during manual segmentation of cristae (i.e., only clearly discernible cristae membranes were included). Segmentation

of each of these mitochondrial components revealed discrete morphological changes between the inner and outer membranes. Most notably, two key distinctions were observed between the outer membrane and the adjacent IBM at the narrowed mitochondrial tip in the adjoining axon segment. First, in some instances the IBM was observed to maintain apposition to the outer membrane at the narrowed mitochondrial tip entering the axon (**Fig. 4A**). Both the inner (orange) and outer (green) membranes can be seen narrowing as they enter the restricted axonal space. Interestingly, cristae (pink) are largely absent from this narrowed portion of the mitochondrion (~69 nm in diameter) residing in the axon. Second, the outer membrane was observed to separate from the inner membrane, leaving a space free of the inner membrane and matrix of the mitochondrion (**Fig. 4B**). In this case, the outer membrane appears to be pulled or stretched into the axon, separated from the other membranes. Thus, it appears the inner mitochondrial membrane has not yet begun to remodel in response to the rather dramatic extension evident in the outer membrane in adaptation to the restricted space within the axon. **Movie S4** shows the segmented model of the three mitochondria in **Figure 3D**. Both representations of inner and outer membrane morphological changes can be seen within the axon.

## Discussion

Although the molecular mechanisms of axonal transport of mitochondria have been widely studied, the potential adaptation of these large organelles to restricted physical dimensions and available space within axons has not been discussed (Morris, 1995; Schwarz, 2013; Zu-Heng Shang, 2017). The current study provides insight into spatial environments within thin axons and presynaptic varicosities of cryopreserved hippocampal neurons in native state by employing 3D cryo-electron tomography. Major morphological adaptations of mitochondria were revealed due to restrictive changes in available space between large presynaptic varicosities and thin axonal segments. To our knowledge, this is the first study to describe such a dramatic alteration of mitochondrial morphology determined by the physical boundaries of axon morphology. Additionally, the segmented 3D reconstruction of mitochondrial ultrastructure revealed distinct alterations between the inner and outer mitochondrial membranes, suggesting differential adaptation of each membrane to spatial restrictions imposed by axon dimensions.

Axon morphology can be widely variable depending on brain region. *En passant* boutons are common in axons of the hippocampus and cortex, giving rise to

heterogeneous axons morphologies with presynaptic varicosities distributed along thin unmyelinated axons (3-7). As axons and synaptic varicosities are dynamic, heterogeneous environments that can be occupied by organelles and molecules differing in size and number, it is important to consider whether available space within the axon may constrain transport of large cargo, such as mitochondria. Using the artifact-free advantages of cryo-ET, we were able to capture the native spatial environments in thin axons and presynaptic varicosities of cultured hippocampal neurons to examine organelle characteristics and distribution. In presynaptic varicosities, organelle populations were diverse in occurrence and number and were distributed with no apparent hindrance due to spatial constraints. However, crowding did appear more evident in proximity to the narrowing at the varicosity/axon boundary. Organelle morphology appeared generally unperturbed within or near this region, with the exception of mitochondria. It is possible that this observation can be attributed to the small relative size of most organelles, vesicles and microtubules, or the amorphous/flexible nature of the ER, which would not face a spatial challenge when entering or exiting the small axonal space. Mitochondria, however, at an average of 250 nm in diameter, presented a clear spatial challenge to reside within axons that are, on average, three times smaller (~80 nm). In the 3D segmentation of mitochondria residing at the boundary between the larger presynaptic varicosity and thin adjoining axon segment we observed mitochondria displaying distinct morphological adaptations to the drastic change in available space. This morphological adaptation was characterized by a normal morphology within the varicosity and a narrowing and thinning of the mitochondrion creating a “tip” that existed in the narrowed space within the axon. Interestingly, in some cases this narrowed portion of the mitochondrion was smaller than the boundary of the axonal plasma membrane, suggesting that additional material, not apparent in the tomograms, might further constrain the space within the axon to influence this morphological adaptation. Furthermore, a more exaggerated example was also observed in which a mitochondrion residing in two varicosity compartments bridged by a narrow (~ 100 nm in length) axon segment (**Fig. 3B**). This mitochondrion appeared forced into a “dumbbell” fashion with two bulbous ends residing in the large varicosity and a narrow “bar-like” structure through the axon. These observations highlight the potential of mitochondrial morphological adaptations to available space within axons with corresponding morphology changes within each compartment.

The importance of mitochondrial axonal transport and synaptic localization to support neuronal function is well recognized (for reviews see (17, 18, 24)). Mitochondria must

traffic through axons to populate distal synapses and mitigate local energy depletion that cannot be supported either by glycolysis or diffusion of ATP from somal compartments (16, 25, 26). Additionally, mitochondrial localization at presynaptic sites is also critical for the regulation of synaptic calcium that controls vesicle release and recycling (19, 25, 27). Thus, disruptions in mitochondrial transport can be detrimental to synaptic communication, plasticity, and survival, and have been implicated in several neurodegenerative processes (reviewed in (17, 28, 29)). The current study highlights the potential implications for spatial restrictions dictated by axon morphology to impact mitochondrial trafficking through the axon. At the cellular level, impediments may occur causing potential axonal "traffic jams" and the accumulation of transported cargo on microtubules that disrupts critical signaling for synaptic function and health (30, 31). In fact, aberrant tau-induced disruptions in axonal trafficking have long been considered as major contributors to neurodegeneration in Alzheimer's disease (32, 33). Additionally, impediments may occur at the mitochondrial level when considering the physical ability of mitochondria to undergo morphological adaptations to restricted space within axons. Specifically, the fluidity and elasticity of mitochondrial membranes may be critical for the physical shaping of mitochondria in thin axons and is proposed to be important for membrane bending and cristae invagination at the inner membrane (34, 35). Furthermore, lipid composition and lipid-protein interactions have been found to be altered in the aging brain and in some neurodegenerative diseases, potentially reducing the ability for mitochondrial membrane reshaping events critical for efficient transport (36-38). Investigation into the composition of inner and outer mitochondrial membranes found in axons would be informative and might provide insights into how mitochondria adapt for transport within the available space within axons.

Cargo within axons are trafficked via motor protein-driven transport on microtubules that create the driving force necessary to pull organelles through the cytoplasm in axons and varicosities (11, 39). Specifically, kinesin and dynein motor proteins exert a mechanical force on the mitochondrion to drive polarity-directed transport through interactions with outer mitochondrial membrane and adaptor proteins, such as Miro and Milton (28). Directional forces induced by motor proteins may drive the morphological stretching of the mitochondrial membrane during transport, as observed in the current study. Kinesins, in particular, are known to induce membrane deformation or tubulation in *in vitro* reconstituted membranes (40, 41). A recent study also described similar thin tubulation of mitochondria that is mediated by KIF5B, a member of the kinesin family involved in mitochondrial transport (42). Interestingly, the influence of mechanical forces

on mitochondrial membrane dynamics was recently demonstrated by the recruitment of mitochondrial fission machinery and subsequent division at sites of induced physical constriction (43). Whether force-driven microtubule transport plays a role in the distinct morphological changes of mitochondria in axons observed in our cryopreserved tomographic reconstructions is an interesting possibility. Thus, further investigation into the precise mechanisms involved in mitochondrial membrane morphology changes preceding or coincident with axonal transport is warranted.

Mitochondria are ancient double membrane-bound organelles and are the major site of ATP synthesis via oxidative phosphorylation. Mitochondrial function is highly dependent on the unique architecture of the inner mitochondrial membrane (IMM), in which the respiratory complexes along with ATP synthase are concentrated in formations of distinct compartments, termed cristae (34, 44-46). Classic and more recent studies examining inner membrane morphology and cristae formation have shown rapid and significant ultrastructural remodeling in response to cellular energy demands, however whether inner membrane structure changes occur correspondingly with gross morphological changes (excluding those involved in mitochondrial fission or fusion) is not well defined (35, 46-51). Therefore, we questioned whether the significant reduction in size of mitochondria in adaptation to axonal space also affected the internal structure of the mitochondria. Segmentation of cristae and the inner boundary membrane (IBM), distinct components of the IMM, revealed divergent characteristics of the relationship between internal structure and the outer mitochondrial membrane (OMM). In some cases, the IBM remained in close apposition with the OMM at the narrowed tip of the mitochondrion in the axon, following the overall gross morphological change. Interestingly, this area was also void of cristae, whereas cristae structure remained unperturbed in the portion of the mitochondrion that resided in the varicosity space, suggesting possible differential regulation of cristae compartments in response to spatial constrictions. Conversely, a few mitochondria displayed a dissociation of the inner and outer mitochondrial membrane, in which the outer membrane is pulled away from the IMM in the narrowed tip of the mitochondrion, creating a “matrix-free” space. The IBM and cristae remained intact and unperturbed within the portion of the mitochondrion residing in the varicosity. The visualization of the 3D ultrastructure of mitochondria undergoing these drastic morphological changes in axons suggests a potentially new instance of structural remodeling of the IMM that is driven by constraints of available space within axons. Mechanistically, this observation generates several interesting questions to the regulation and dynamic nature of mitochondrial

ultrastructure, as well as the functional status of mitochondria during this adaptation. Although mechanisms for regulating inner membrane morphology remain incompletely defined, recent research has provided insight into some mechanisms involved in regulation cristae structure and IMM morphology (34, 47, 52, 53). In addition to Opa1, the primary IMM fusion protein, ATP synthase and the mitochondrial contact site and cristae organizing system (MICOS) exhibit membrane bending functions and are proposed to determine curvature of the cristae membrane (34, 35). MICOS components have also been implicated in regulating cristae morphology, as well as inner-outer membrane tethering, which could be a potential mechanism driving the differences in inner-outer membrane apposition or dissociation observed in the present study (54, 55). Moreover, distinct events of IMM constriction independent from the OMM have also recently been observed that are driven by increased mitochondrial matrix calcium levels (56-58). Thus, there is some evidence at the cellular level for differential morphological regulation of the inner and outer membranes. The 3D reconstructions of the OMM, IBM, and cristae in the intact, cryo-preserved axon, and the observed dissociation between membrane morphologies in the current study lends support for the notion that the OMM and IMM can be remodeled independently. Functionally, the observed changes in cristae and IMM morphology also pose the question to whether the lack of cristae or adaptation of the IMM to spatial constraints influence the functional capacity of trafficking mitochondria. Although the technical limitations of measuring mitochondrial function in relation to mitochondrial structure are challenging, these will be critical investigations in uncovering the dynamic and adaptive nature of the IMM and regulation of mitochondrial function in axons.

In conclusion, our cryo-ET study revealed major morphological adaptations of mitochondria to restricted physical dimensions dictated by changes in axon morphology. Furthermore, the segmentation of mitochondrial membranes revealed distinct morphological changes between the inner and outer mitochondrial membranes during this adaptation, suggesting independent regulation of each membrane to spatial constraints within axons. These findings offer new perspectives on the physical and spatial influence of the cellular environment on mitochondrial morphology and highlights the remarkable structural plasticity of mitochondria to navigate the limited available space during axonal transport. Given the importance of membrane structure for mitochondrial function and the necessary transport of mitochondria for maintaining synaptic health and neurotransmission, these findings have far reaching implications for mitochondrial and neuronal biology. Future research will be essential to gain mechanistic insight to

regulation of structural changes at mitochondrial membranes and the influence of morphological adaptations of mitochondria during axonal transport.

## Materials and Methods

### Neuronal Culture and Cryopreservation

Primary neuronal cultures were prepared from E18 rat hippocampi. All protocols involving vertebrate animals were approved by the Institutional Animal Care and Use Committee prior to initiating the studies. Briefly, pooled hippocampi were digested with papain for 20 min at 37°C and then triturated with a 10 ml pipet. Cells were counted and diluted in Opti-MEM containing 20 mM glucose to a density of 1.5 x $10^5$/ml. 200 mesh gold grids covered with Quantifoil 2/1 carbon were placed in 35 mm glass bottom Mat-Tek dishes and were treated overnight with 100 ug/ml poly-D-lysine. The dishes were then washed 3x with sterile water before plating cells at a density of 1.5 x $10^6$/dish. After letting the cells attach for 1 hr at 37°C/5%$CO_2$, the media was exchanged for Neurobasal A supplemented with 2% B-27 (Life Technologies), GlutaMAX (Thermo Scientific, Waltham, CA), and penicillin-streptomycin (Sigma, St. Louis, MO) and incubated for 10 d at 37°C/5%$CO_2$.

To cryopreserve intact neurons, the grids were lifted from the Mat-Tek dishes and 5 uL of Neurobasal media containing BSA coated 10 nm gold fiducials was applied. After manual blotting, the grids were plunged into liquid ethane cooled with liquid $N_2$. Cryo-preserved grids were stored in liquid $N_2$ until use.

### Immunocytochemistry

Immunostaining of neurons grown on Quantifoil grids was accomplished by fixing the neurons at 10 d post-plating in freshly prepared 4% paraformaldehyde in 0.1 M phosphate buffer, pH 7.4, for 10 min at room temperature. The fixative was removed and reaction quenched with a 5 min incubation in 50 mM glycine in 0.1 M phosphate buffer, pH 7.4. Neurons were permeabilized with 0.5% TX-100 in 0.1 M phosphate buffer, pH 7.4, for 15 min and then non-specific sites blocked with Blocking buffer (2% normal goat serum, 1% bovine serum albumin, 0.1% TX-100 in 0.1 M phosphate buffer, pH 7.4) for 30 min. Primary antibodies were diluted 1:1000 in Blocking buffer and incubated for 1 hr at room temp. Primary antibodies included a monoclonal antibody to CaMKII$\alpha$ (created in

our lab; (59)) and a rabbit polyclonal antibody to synapsin 1 (Synaptic Systems Inc.). Grids were then washed 3x, 5 min each, with Wash buffer (0.2% normal goat serum, 0.1% bovine serum albumin, 0.01% TX-100 in 0.1 M phosphate buffer, pH 7.4). Grids were then incubated in 1:500 dilution of Alexa 488 labeled goat anti-mouse IgG and Alexa 568 labeled goat anti-rabbit IgG diluted in Blocking buffer for 30 min at room temperature. Grids were washed 3x 5 min each in Wash buffer, once in 0.1 M phosphate buffer, pH 7.4 and then mounted in Fluoromount anti-fade mounting compound. Bright field and fluorescent images were collected with a 10x, or 40x magnification using a 0.9 NA water immersion lens on a Zeiss inverted microscope using an Andor Zyla 4.0 CMOS camera. Exposure time, shutter and filter wheel (Sutter) were controlled through Metamorph software (Molecular Devices).

Cryo-electron Tomography

For tomographic data collection, single-axis tilt series were collected from -50° to +50° in 3° increments at approximately -8 □m under focus on an FEI Polara G2 operated at 300 kV equipped with a Gatan K2 Summit direct electron detector operated in photon counting mode. Data collection was performed in a semi-automated fashion using Serial EM software operated in low-dose mode (60). Briefly, areas of interest were identified visually and 8 x 8 montages were collected at low magnification (2400x) and then individual points were marked for automated data collection. Data was collected at either 8.5 or 4.5 Å/pixel. Movies of 8-10 dose-fractionated frames were collected at each tilt angle and the electron dose spread across all images was limited to a total dose of < 100 $e^-/Å^2$ per tilt series.

Tomographic Reconstruction and Segmentation

Each tomographic data set was drift corrected with MotionCorr2 (61) and stacks were rebuilt and then aligned using IMOD (62, 63). Tomograms of the aligned stacks were then reconstructed using TOMO3D (64, 65). Contrast was enhanced using SIRT reconstruction implemented in TOMO3D. Tomograms will be deposited in the Electron Microscopy Data Bank.

Reconstructed tomograms were further processed using the median, non-local means, and lanczos filters in Amira (FEI, ThermoFisher Scientific) for manual and semi-automated segmentation. Segmentation was accomplished using images displayed in the X, Y, and Z dimensions. The brush tool was primarily used in manual segmentation and

masking approaches in combination with density thresholding was used for semi-automated segmentation when possible. After segmentation, smoothing tools were employed and surfaces were rendered for model construction. All measurements (length and diameter) were performed in either Amira using the 3D measurement tool or in IMOD.

**Acknowledgements**

The authors would like to acknowledge Dr. Andrey Tsvetkov, Ndidi Uzor and Felix Moruno Manchon for help with primary neuronal cultures. We would also like to thank Dr. Richard Youle and Dr. Matt Swulius for advice on the manuscript. This study was supported by grants from the National Institute of Health/National Institute of Neurological Disease and Stroke; R01NS101686 (MWN and PKD), R01NS087149 (PKD) and F31NS098790, Ruth L. Kirchstein National Research Service Award Predoctoral Fellowship (TF). PKD acknowledges support from the Nina and Michael Zilkha endowment and MNW acknowledges support from the William Wheless III professorship. The Polara electron microscope was supported, in part, through the Structural Biology Imaging Center at UTHSC—Houston. The Gatan K2 Summit was funded by the National Institutes of Health—Award S10OD016279.

## References


1. Debanne D (2004) Information processing in the axon. *Nature Reviews Neuroscience* 5:304-316.
2. Ishizuka N, Weber J, & Amaral DG (1990) Organization of intrahippocampal projections originating from CA3 pyramidal cells in the rat. *The Journal of Comparative Neurology* 295:580-623.
3. Li X-G, Somogyi P, Ylinen A, & Buzsáki G (1994) The hippocampal CA3 network: An in vivo intracellular labeling study. *Journal of Comparative Neurology* 339:181-208.
4. Shepherd GM & Harris KM (1998) Three-dimensional structure and composition of CA3-->CA1 axons in rat hippocampal slices: implications for presynaptic connectivity and compartmentalization. *J Neurosci* 18(20):8300-8310.
5. Westrum LE & Blackstad TW (1962) An electron microscopic study of the stratum radiatum of the rat hippocampus (regio superior, CA 1) with particular emphasis on synaptology. *J Comp Neurol* 119:281-309.
6. Muller D & Nikonenko I (2003) Dynamic presynaptic varicosities: A role in activity-dependent synaptogenesis. *Trends in Neurosciences* 26:573-575.
7. Shepherd GMG, Raastad M, & Andersen P (2002) General and variable features of varicosity spacing along unmyelinated axons in the hippocampus and cerebellum. *Proceedings of the National Academy of Sciences* 99:6340-6345.
8. Berbel P & Innocenti GM (1988) The development of the corpus callosum in cats: a light- and electron-microscopic study. *J Comp Neurol* 276(1):132-156.
9. Anderson JC & Martin KAC (2001) Does bouton morphology optimize axon length? *Nature Neuroscience* 4:1166-1167.
10. Conde C & Cáceres A (2009) Microtubule assembly, organization and dynamics in axons and dendrites. *Nature Reviews Neuroscience* 10:319-332.
11. Saxton WM & Hollenbeck PJ (2012) The axonal transport of mitochondria. *Journal of Cell Science* 125:2095-2104.
12. Fernández-Busnadiego R*, et al.* (2011) Insights into the molecular organization of the neuron by cryo-electron tomography. *Journal of Electron Microscopy* 60:137-148.
13. Siksou L*, et al.* (2007) Three-Dimensional Architecture of Presynaptic Terminal Cytomatrix. *Journal of Neuroscience* 27:6868-6877.
14. Palade G (1952) The fine structure of mitochondria. *The Anatomical record* 114:427-451.
15. Frey TG & Mannella CA (2000) Mannella - The Internal Structure of Mitochondria. 0004:1-6.
16. Rangaraju V, Calloway N, & Ryan TA (2014) Activity-driven local ATP synthesis is required for synaptic function. *Cell* 156:825-835.
17. Devine MJ & Kittler JT (2018) Mitochondria at the neuronal presynapse in health and disease. *Nature Reviews Neuroscience* 19:63-80.
18. Sheng ZH (2017) The Interplay of Axonal Energy Homeostasis and Mitochondrial Trafficking and Anchoring. *Trends in Cell Biology* 27:403-416.
19. Sun T, Qiao H, Pan PY, Chen Y, & Sheng ZH (2013) Motile axonal mitochondria contribute to the variability of presynaptic strength. *Cell Reports* 4:413-419.
20. Li Z, Okamoto KI, Hayashi Y, & Sheng M (2004) The importance of dendritic mitochondria in the morphogenesis and plasticity of spines and synapses. *Cell* 119:873-887.

21. Wu Y*, et al.* (2017) Contacts between the endoplasmic reticulum and other membranes in neurons. *Proceedings of the National Academy of Sciences* 114:E4859-E4867.
22. Chen X*, et al.* (2008) Organization of the core structure of the postsynaptic density. *Proceedings of the National Academy of Sciences* 105:4453-4458.
23. Grabrucker A, Vaida B, Bockmann J, & Boeckers TM (2009) Synaptogenesis of hippocampal neurons in primary cell culture. *Cell Tissue Res* 338(3):333-341.
24. Misgeld T & Schwarz TL (2017) Mitostasis in Neurons: Maintaining Mitochondria in an Extended Cellular Architecture. *Neuron* 96:651-666.
25. Verstreken P*, et al.* (2005) Synaptic Mitochondria Are Critical for Mobilization of Reserve Pool Vesicles at Drosophila Neuromuscular Junctions. *Neuron* 47:365-378.
26. Pathak D, Berthet A, & Nakamura K (2013) Energy Failure : Does It Contribute to Neurodegeneration ?
27. Billups B & Forsythe ID (2002) Presynaptic mitochondrial calcium sequestration influences transmission at mammalian central synapses. *The Journal of neuroscience : the official journal of the Society for Neuroscience* 22:5840-5847.
28. Sheng Z-H & Cai Q (2012) Mitochondrial transport in neurons: impact on synaptic homeostasis and neurodegeneration. *Nature reviews Neuroscience* 13:77-93.
29. Itoh K, Nakamura K, Iijima M, & Sesaki H (2013) Mitochondrial dynamics in neurodegeneration. *Trends in Cell Biology* 23:64-71.
30. Kuznetsov AV & Avramenko AA (2009) A macroscopic model of traffic jams in axons. *Mathematical Biosciences* 218:142-152.
31. Leduc C*, et al.* (2012) Molecular crowding creates traffic jams of kinesin motors on microtubules. *Proceedings of the National Academy of Sciences* 109.
32. Shemesh OA, Erez H, Ginzburg I, & Spira ME (2008) Tau-induced traffic jams reflect organelles accumulation at points of microtubule polar mismatching. *Traffic* 9:458-471.
33. Conway L, Wood D, Tuzel E, & Ross JL (2012) Motor transport of self-assembled cargos in crowded environments. *Proceedings of the National Academy of Sciences* 109:20814-20819.
34. Davies KM, Anselmi C, Wittig I, Faraldo-Gomez JD, & Kuhlbrandt W (2012) Structure of the yeast F1Fo-ATP synthase dimer and its role in shaping the mitochondrial cristae. *Proceedings of the National Academy of Sciences* 109:13602-13607.
35. Tarasenko D*, et al.* (2017) The MICOS component Mic60 displays a conserved membrane-bending activity that is necessary for normal cristae morphology. *The Journal of Cell Biology* 216:889-899.
36. Pollard AK, Ortori CA, Stöger R, Barrett DA, & Chakrabarti L (2017) Mouse mitochondrial lipid composition is defined by age in brain and muscle. *Aging* 9:986-998.
37. Kennedy MA*, et al.* (2016) A Signaling Lipid Associated with Alzheimer's Disease Promotes Mitochondrial Dysfunction. *Scientific Reports* 6:19332.
38. Aufschnaiter A*, et al.* (2017) Mitochondrial lipids in neurodegeneration. *Cell Tissue Res* 367(1):125-140.
39. Schwarz TL (2013) Mitochondrial Trafficking in Neurons. *Cold Spring Harbor Perspectives in Biology*:1-15.
40. Vale RD & Hotani H (1988) Formation of membrane networks in vitro by kinesin-driven microtubule movement. *Journal of Cell Biology* 107:2233-2241.
41. Vale RD, Reese TS, & Sheetz MP (1985) Identification of a novel force-generating protein, kinesin, involved in microtubule-based motility. *Cell* 42:39-50.

42. Wang C*, et al.* (2015) Dynamic tubulation of mitochondria drives mitochondrial network formation. *Cell Research* 25:1108-1120.
43. Helle SCJ*, et al.* (2017) Mechanical force induces mitochondrial fission. *eLife* 6:e30292.
44. Pernas L & Scorrano L (2015) Mito-Morphosis: Mitochondrial Fusion, Fission, and Cristae Remodeling as Key Mediators of Cellular Function. *Annual review of physiology* 78:annurev-physiol-021115-105011.
45. Mannella Ca*, et al.* (2001) Topology of the mitochondrial inner membrane: dynamics and bioenergetic implications. *IUBMB life* 52:93-100.
46. Cogliati S*, et al.* (2013) Mitochondrial cristae shape determines respiratory chain supercomplexes assembly and respiratory efficiency. *Cell* 155:160-171.
47. Cogliati S, Enriquez JA, & Scorrano L (2016) Mitochondrial Cristae: Where Beauty Meets Functionality. *Trends in Biochemical Sciences* 41:261-273.
48. Mannella CA (2006) Structure and dynamics of the mitochondrial inner membrane cristae. *Biochimica et Biophysica Acta (BBA) - Molecular Cell Research* 1763:542-548.
49. Hackenbrock CR (1966) Ultrastructural bases for metabolically linked mechanical activity in mitochondria. I. Reversible ultrastructural changes with change in metabolic steady state in isolated liver mitochondria. *J Cell Biol* 30(2):269-297.
50. Hackenbrock CR (1968) Ultrastructural bases for metabolically linked mechanical activity in mitochondria. II. Electron transport-linked ultrastructural transformations in mitochondria. *J Cell Biol* 37(2):345-369.
51. Hackenbrock CR & Caplan AI (1969) Ion-induced ultrastructural transformations in isolated mitochondria. The energized uptake of calcium. *J Cell Biol* 42(1):221-234.
52. Kühlbrandt W (2015) Structure and function of mitochondrial membrane protein complexes. *BMC biology* 13:89.
53. Friedman JR, Mourier A, Yamada J, Michael McCaffery J, & Nunnari J (2015) MICOS coordinates with respiratory complexes and lipids to establish mitochondrial inner membrane architecture. *eLife* 2015:1-61.
54. Harner ME*, et al.* (2016) An evidence based hypothesis on the existence of two pathways of mitochondrial crista formation. *eLife* 5:1-25.
55. Zerbes RM*, et al.* (2012) Mitofilin complexes: Conserved organizers of mitochondrial membrane architecture. *Biological Chemistry* 393:1247-1261.
56. Chakrabarti R*, et al.* (2018) INF2-mediated actin polymerization at the ER stimulates mitochondrial calcium uptake , inner membrane constriction , and division. *Journal of Cell Biology*:1-18.
57. Cho B*, et al.* (2017) Constriction of the mitochondrial inner compartment is a priming event for mitochondrial division. *Nature Communications* 8:15754.
58. Lee H & Yoon Y (2014) Transient contraction of mitochondria induces depolarization through the inner membrane dynamin opa1 protein. *Journal of Biological Chemistry* 289:11862-11872.
59. Waxham MN, Aronowski J, & Kelly PT (1989) Functional analysis of Ca2+/calmodulin-dependent protein kinase II expressed in bacteria. *J Biol Chem* 264(13):7477-7482.
60. Mastronarde DN (2005) Automated electron microscope tomography using robust prediction of specimen movements. *J Struct Biol* 152(1):36-51.
61. Zheng SQ*, et al.* (2017) MotionCor2: anisotropic correction of beam-induced motion for improved cryo-electron microscopy. *Nat Methods* 14(4):331-332.
62. Kremer JR, Mastronarde DN, & McIntosh JR (1996) Computer visualization of three-dimensional image data using IMOD. *J Struct Biol* 116(1):71-76.

63. Mastronarde DN & Held SR (2017) Automated tilt series alignment and tomographic reconstruction in IMOD. *J Struct Biol* 197(2):102-113.
64. Agulleiro JI & Fernandez JJ (2011) Fast tomographic reconstruction on multicore computers. *Bioinformatics* 27(4):582-583.
65. Agulleiro JI & Fernandez JJ (2015) Tuning the cache memory usage in tomographic reconstruction on standard computers with Advanced Vector eXtensions (AVX). *Data Brief* 3:16-20.

**Figure Legends**

Figure 1. Growth and characterization of primary hippocampal neurons on EM grids. Hippocampal neurons were isolated from E18 rats and plated on poly-D-lysine coated Quantifoil 2/1 gold grids. A) Low magnification bright field image showing the typical distribution of neuronal soma and processes after 10 d in culture. B) Higher magnification image of the area from the white box in panel (A) with neuronal processes highlighted by white brackets. (C) Wide-field fluorescence image showing immunolabeling of the neuron specific protein CaMKII$\alpha$ in green and the presynaptic vesicle associated protein synapsin 1 in red. The blue color is from a bright field overlay of the same area that also highlights the bars of the EM grid. (D) Higher magnification image in a different area of the same immunolabeled grid highlighting the punctate staining of synapsin I (red; arrowheads) along processes typical of *en passant* varicosities in hippocampal axons. Blue is again from where the grid bars and holes in the Quantifoil grid are apparent. Scale bars in panels A-C = 100 $\mu$m and in panel D = 50 $\mu$m. (E) Low magnification montage of one area in a cryopreserved grid of hippocampal neurons 10 d post-plating showing the typical distribution of axons and synaptic varicosities. Scale bar = 10 $\mu$m. F) Higher magnification representation from (E; white box) showing the axon and varicosity distribution overlying carbon (slightly darker areas) and grid holes. Examples of varicosities lying within grid holes are marked with white asterisks while examples lying on the carbon are marked with red asterisks. Axon segments interconnecting the varicosities are highlighted with black brackets. Scale bar = 2 $\mu$m.

Figure 2. Tomographic reconstruction of a typical pre-synaptic varicosity and adjoining axon segment. A) 2D slice from the tomographic reconstruction showing the distribution of organelles in the varicosity PM: plasma membrane, MT: microtubules, Mito: mitochondria, ER: endoplasmic reticulum, Ves: vesicle, MVB: multi-vesicular body, Golgi: Golgi body. Scale bar = 200 nm. B) Segmented representation of the entire 3D tomogram volume shown in (A) revealing the relative size and spatial distribution of the organelle environment in the varicosity and axon segment. Plasma membrane (dark blue), microtubules (light blue), mitochondrial outer membrane (dark green), endoplasmic reticulum (yellow), vesicles (dark purple), multi-vesicular body (light purple), Golgi body (pink). Scale bar = 200 nm.

Figure 3. Mitochondria undergo major morphological changes to adapt to axonal spatial constraints. A-D) Four different 3D segmented reconstructions showing representative examples of mitochondria residing partially in the varicosity and adjoining axon segments, demonstrating different states of transition into the restricted space of the axon segment. Additional organelles occupying the axon space are also segmented. For clarity, organelles and other structures in the varicosity are not shown. Plasma membrane (dark blue), microtubules (light blue), mitochondrial outer membrane (dark green), endoplasmic reticulum (yellow), vesicles (dark purple).

Figure 4. Morphological adaptations of the mitochondrial membranes to accommodate restricted axonal spatial constraints. A-B) To highlight the membrane organization of the mitochondria shown in Figure 3A and 3D, the cristae and inner and outer membranes of the 3D reconstructions were segmented. A) Mitochondrial inner and outer membranes remain in close apposition within the narrowed portion of this mitochondrion resident in the axon. B) Mitochondrial outer membrane is pulled away from the inner membrane, creating a distinct compartment in this portion of the mitochondria resident in the axon. Plasma membrane (dark blue), mitochondrial outer membrane (dark green), mitochondrial inner boundary membrane (orange), cristae (pink).

Supporting Figure Legends

Figure S1. 2D slices from tomographic reconstructions of different membrane bound organelles observed in the varicosities of cryopreserved hippocampal neurons. A) mitochondrion, B) MVB and vesicles (arrowheads). C) ER and Golgi, D) Autophagosome, E) Lamellar body. Scale bar = 200 nm.

Figure S2. Different mitochondrial cristae ultrastructures in varicosities. A) Representations of mitochondria displaying thin, lamellar cristae. B) Representations of mitochondria displaying thick, unstructured cristae. Scale bar = 200 nm.

Movie S1. Animation of the 3D tomographic reconstruction and overlay of the segmented structures in Figure 1C. Scale bar = 200 nm.

Movie S2. Amination of the microtubule occupation and available space within an axon. Animation and overlay of segmented microtubules in an axon presented moving along the X dimension. Scale bar = 200 nm.

Movie S3. Animation of the 3D tomographic reconstruction and overlay of the segmented structures in Figure 3A. Scale bar = 200 nm.

Movie S4. Animation of the 3D tomographic reconstruction and overlay of the segmented membranes of mitochondria in Figure 3D. Scale bar = 200 nm.

Figure 1

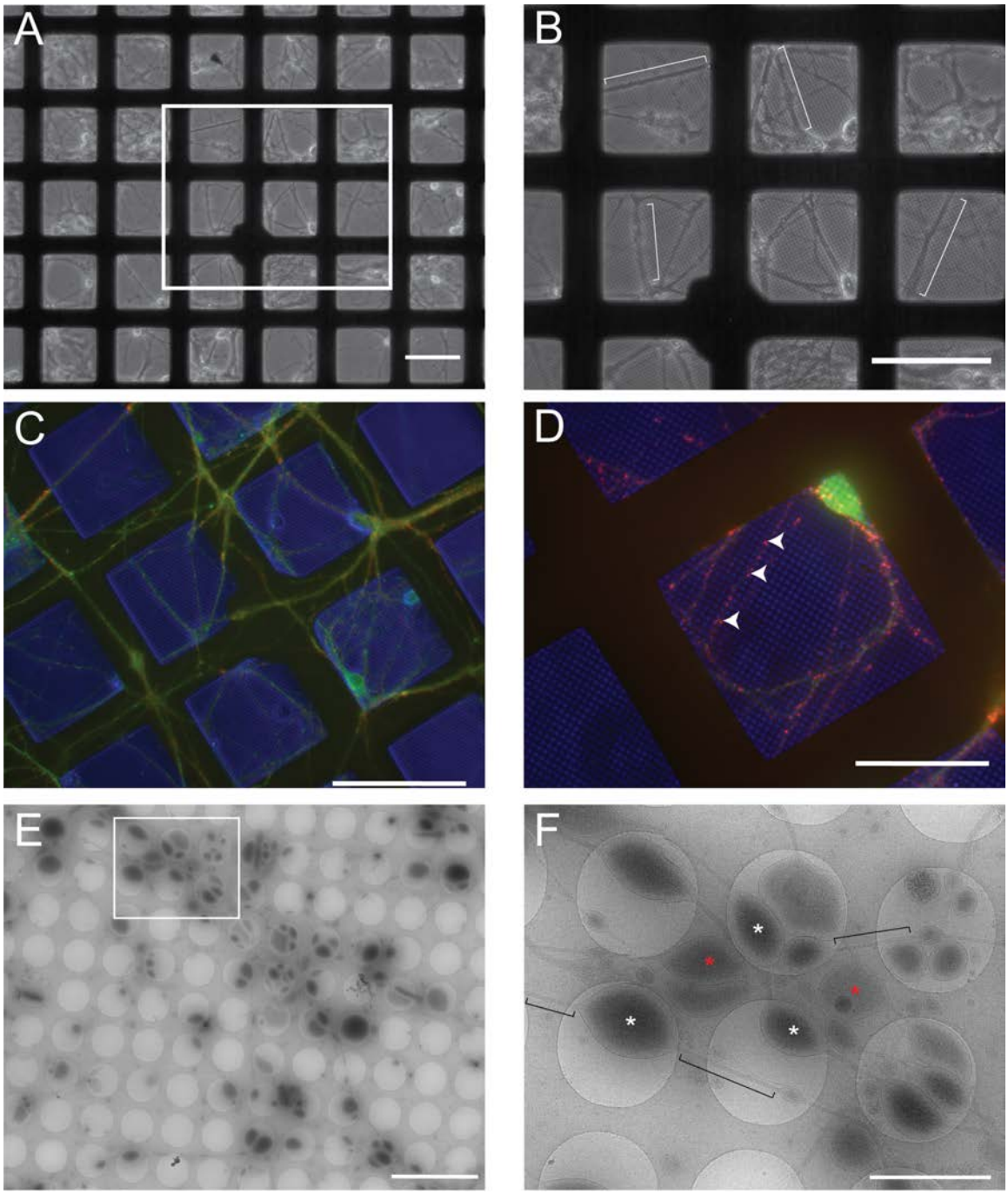

Figure 2

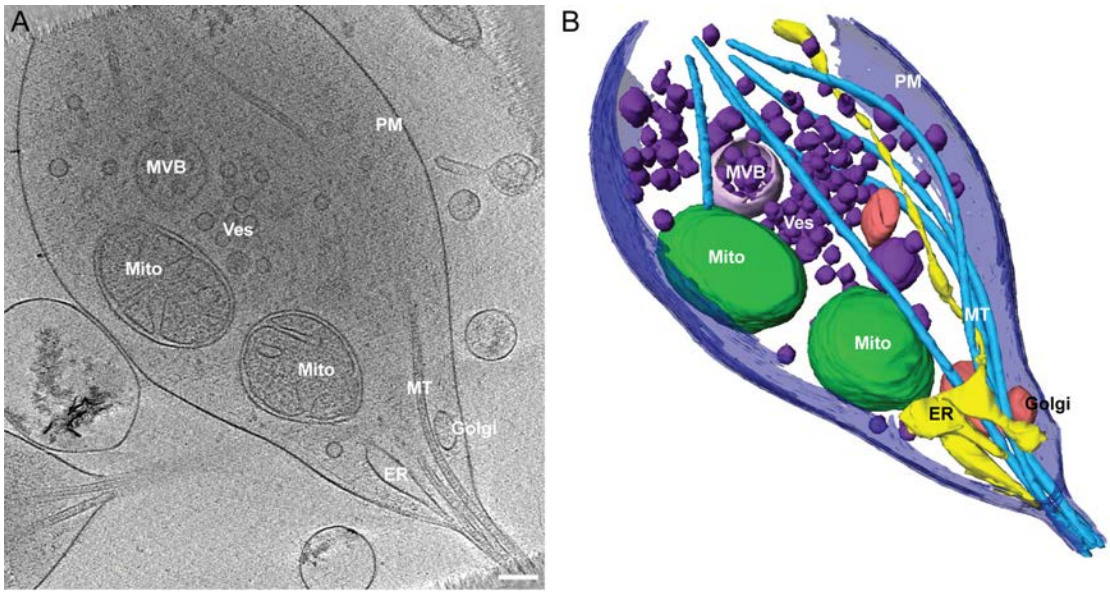
A
PM
MVB
Ves
Mito
Mito
MT
Golgi
ER
B
PM
MVB
Ves
Mito
Mito
MT
ER
Golgi

Figure 3

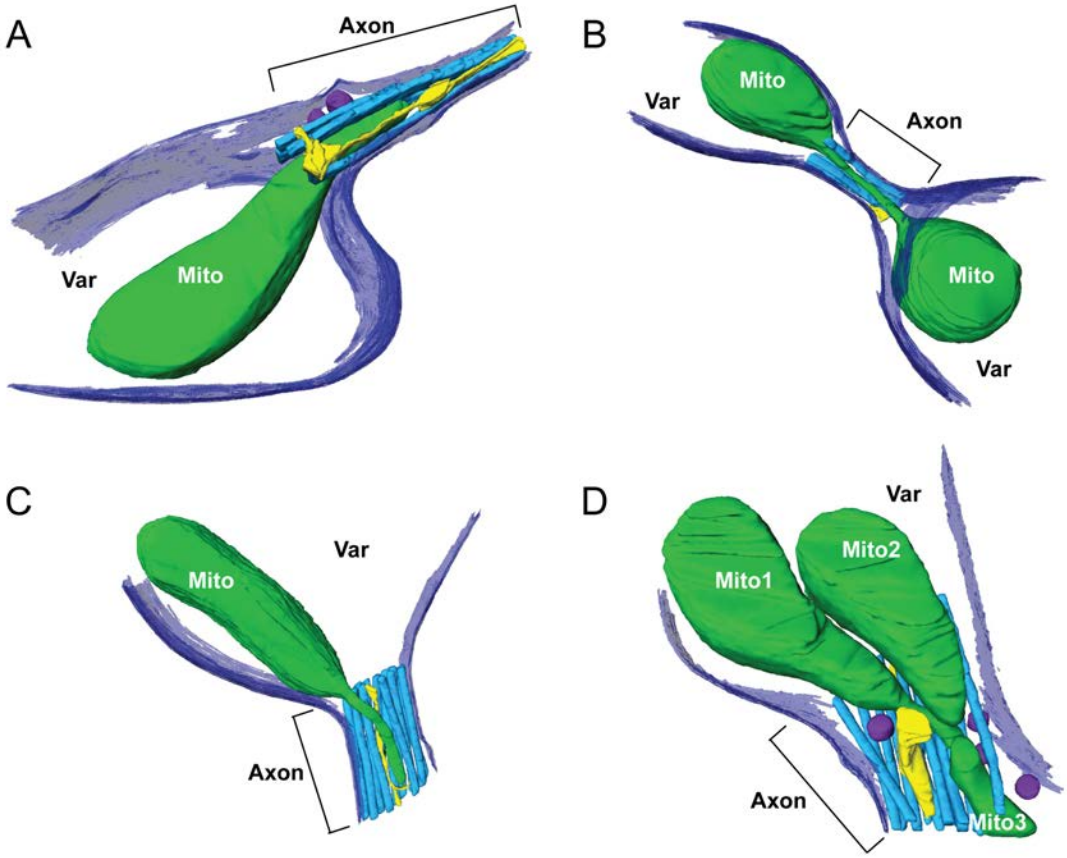
A
Axon
Var
Mito
B
Mito
Var
Axon
Mito
Var
C
Var
Mito
Axon
D
Var
Mito2
Mito1
Axon
Mito3

Figure 4

A

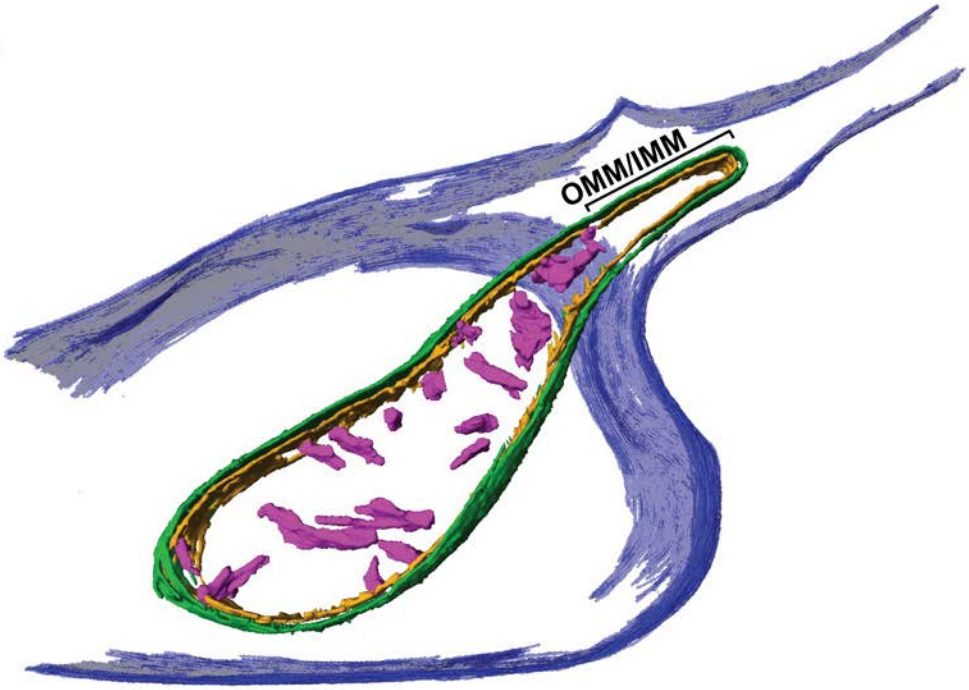


B

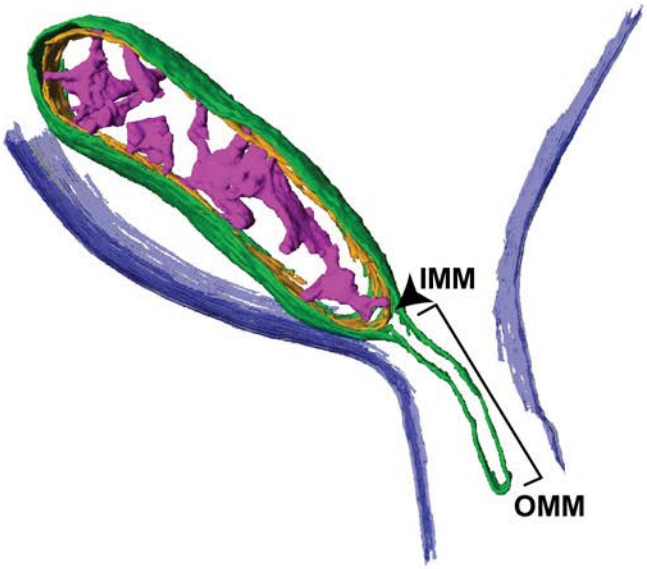

Figure S1

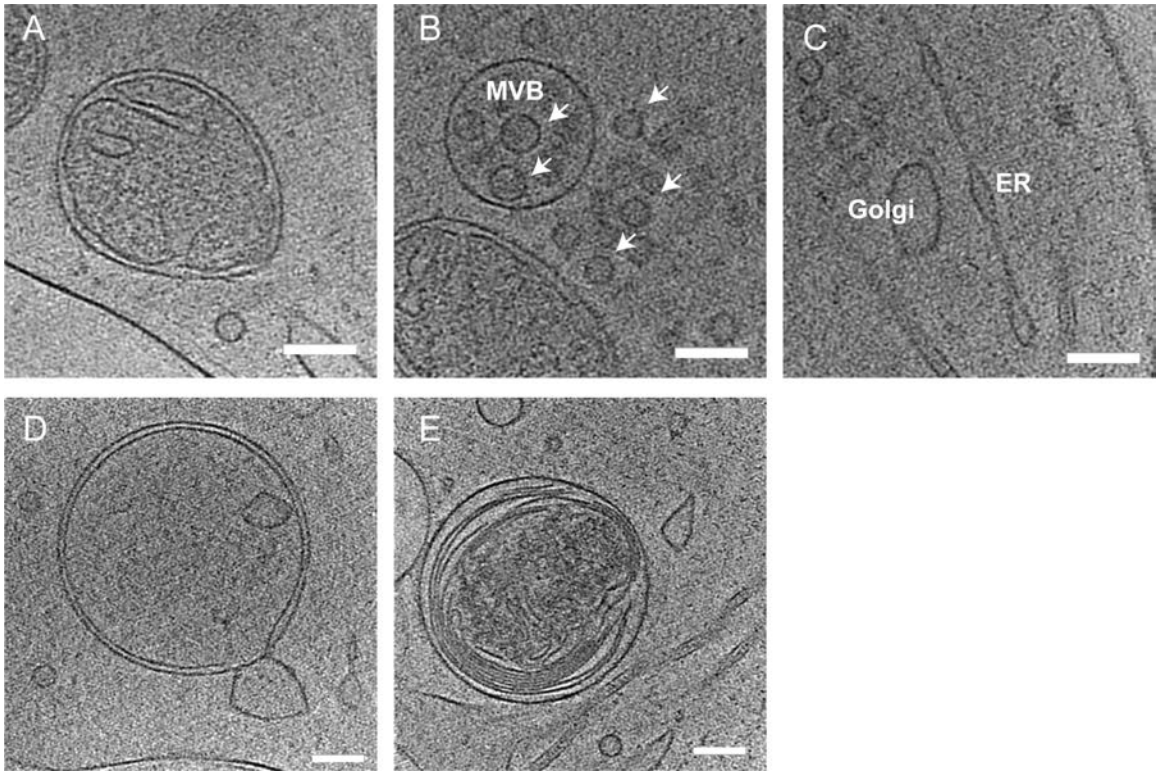
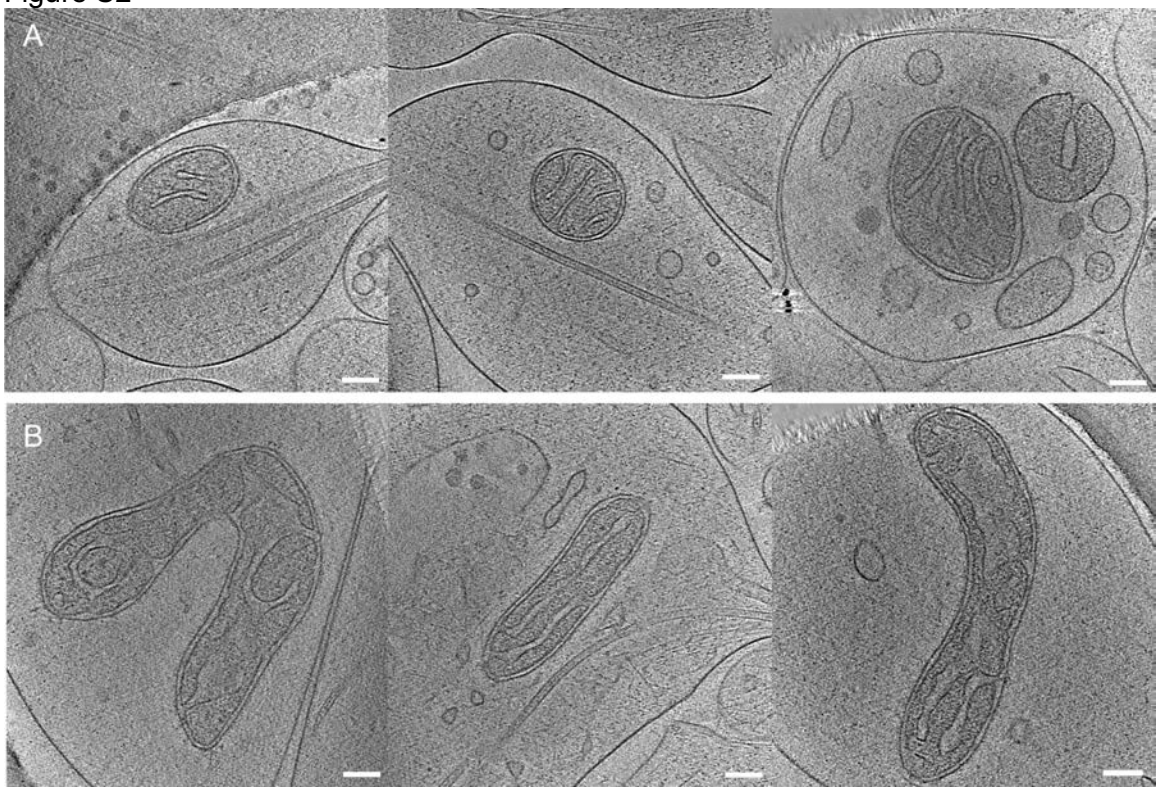
Figure S2